

# Sparse phase imaging based on complex domain nonlocal BM3D techniques

Vladimir Katkovnik\*, Karen Egiazarian

*Department of Signal Processing, Technology University of Tampere, Tampere, Finland, 33720. Emails: vladimir.katkovnik@tut.fi, karen.egiazarian@tut.fi*

---

## Abstract

The paper is addressed to 2D phase and amplitude estimation of complex-valued signals - that is, in particular, to estimation of modulo- $2\pi$  interferometric phase images from periodic and noisy observations. These degradation mechanisms make phase image estimation a challenging problem. A sparse nonlocal data-adaptive imaging formalized in complex domain is used for phase and amplitude image reconstruction. Following the procedure of patch-based technique, the image is partitioned into small overlapping square patches. Block Matching Three Dimensional (BM3D) technique is developed for forming complex domain sparse spectral representations of complex-valued data. High Order Singular Value Decomposition (HOSVD) applied to BM3D groups enables the design of the orthonormal complex domain 3D transforms which are data adaptive and different for each BM3Ds group. An iterative version of the complex domain BM3D is designed from variational formulation of the problem. The convergence of this algorithm is shown. The effectiveness of the new sparse coding based algorithms is illustrated in simulation experiments where they demonstrate the state-of-the-art performance.

*Key words:* complex domain image denoising, complex domain sparsity, phase imaging, non-local block matching, HOSVD.

---

\*Corresponding author

## 1. Introduction

This paper is focussed on a special wide class imaging problems concerning wavefield/wavefront sensing and reconstruction. In particular, a monochromatic coherent wavefield is modelled by complex amplitude  $u = ae^{j\varphi}$ , where  $a$  is an amplitude and  $\varphi$  is a phase of the wavefield. In modern technology and science phase and wavefield imaging are popular and well established technique for high-accuracy measuring, recording and reconstructing 2D and 3D objects. The areas of applications are varying from astronomy and engineering to medicine and biology [1], [2]. In engineering phase and wavefield sensing methods serve for nondestructive testing/control and precise measurements (e.g. [3] - [6]). In medicine and biology phase measurements are exploited in microscopy and coherent tomography, for instance in Fourier phase microscopy. We wish to mention also such developments as phase based registration of brain dynamics, express blood tests, measurement of biological structures in body tissues.

The phase variations cannot be measured directly because all measurements instruments and sightseeing of human are sensitive with respect to intensity but not to phase of light beams. Accordingly one of the main targets of phase image processing is to extract phase information from measured intensities.

For instance, in interferometry and holography these intensities have a form:

$$I(x) = |u_o(x) + u_r(x)|^2 \quad (1)$$

where  $u_o(x)$  and  $u_r(x)$  stand for object and reference beam wavefronts, respectively, and  $I(x)$  is a measured intensity (power).

For monochromatic coherent imaging both object and reference beams are complex-valued:

$$u_o(x) = a_o \exp(i\varphi_o(x)), \quad u_r(x) = a_r \exp(i\varphi_r(x)). \quad (2)$$

For these models of the object and reference beams the intensity takes the form

$$I(x) = a_o^2(x) + a_r^2(x) + 2 \cos(\varphi_o(x) - \varphi_r(x)). \quad (3)$$

Then, phase imaging means reconstruction of the phase  $\varphi_o(x)$  from usually noisy measurements of  $I(x)$  given for various  $u_r$ . The amplitude  $a_o(x)$  is also unknown and accurate phase reconstruction requires also a reconstruction of  $a_o(x)$ . Accordingly, complex-valued image processing means reconstruction of  
25 both phase and amplitude.

Phase and amplitude may have very different distributions on the argument  $x$ , for instance, with an invariant amplitude and varying phase ("phase object") or vice versa with a varying amplitude and invariant phase ("amplitude object"). Nevertheless, it is quite common that same features can be seen in both phase  
30 and amplitude images. In this case a correlation of phase and amplitude can be used for improved reconstruction.

The topic of sparse and redundant representations in discrete imaging has attracted tremendous interest in the last ten years. This interest is defined by the fundamental role that low dimensional models play in many signal and image processing areas such as compression, restoration, classifications, and design  
35 of priors and regularizers, just to name a few. It is assumed in sparse imaging that there exists a basis consisting of a small number of items where image can be represented exactly or approximately with a good accuracy. This ideal basis is a priory unknown and selected from a given set of potential bases (dictionary  
40 or dictionaries) or designed from given noisy observations. Sparse representation can be treated as regression approximation of signals with an adaptive basis selection, one of the classical topics in statistics. The modern popularity and success of sparse representation are mainly due to efficient algorithms and multiple evidences that this type of mathematical modeling meets requirements of many important applications. Compressive sensing (CS) is one of the  
45 fields where sparse representation techniques are efficient. In CS, the object distribution image is reconstructed from subsampled data. A total number of available observations can be smaller (much smaller) than a size of the image. It is proved in CS that perfect reconstruction from the subsampled data can  
50 be achieved for sparse images. To add yet more interest to this imaging techniques, the dictionaries yielding sparse representations may be learned from the

data they represent. Dictionary learning is currently one of the hottest research topics in the area of sparse imaging [7].

The compressive imaging (CI) uses the same sparse techniques but with  
55 the main intention to achieve the best quality/accuracy from given observation without special intentions to compress data.

Recently in optics, CI in complex domain has become a subject of multiple applications. Complex-valued data and operators are distinctive features of this development. Basic facts of the corresponding theory, algorithms, simulations  
60 as well as experimental demonstrations can be found in [8], [9]. In the works concerning the complex-valued data the phase is the most delicate and difficult issue and, in particular, the corresponding dictionary design for sparse modeling is crucial. One of the first demonstration that the sparsity prior imposed on phase due to the joint quadratic and total variation (TV) penalization results  
65 in the significant complex-valued wavefront reconstruction was done in [10].

A serious accuracy improvement for wavefield reconstruction was demonstrated in [11] - [13] due to a sparse modeling separate for amplitude and absolute phase. A regularization of amplitude and interferometric phase through the total variation penalties is introduced in [14] for wavefield reconstruction in  
70 digital holography.

Complex domain natural signals, exhibit complicated structures, in particular, complicated due to variations both in phase and amplitude. It makes CI as well as design of regularizators for these problems a quite difficult problem.

Recently, it has been demonstrated that denoising algorithms, designed for  
75 additive noise observations, can serve as efficient regularizators in various CI problems as "plug-and-play priors" [15] - [18]. In particular, in these cited papers it was done using as the denoising algorithm the Block Matching 3D (BM3D) filters [19] in this way transfer the CI problem to design of these sparsity based filters.

80 The original BM3D paradigm was proposed for real-valued signals and recently extended to the complex domain [26].

The idea of this generalization is as follows. The complex-valued image is

partitioned into small overlapping rectangular patches. For each patch, a group of similar patches is collected from a pre-defined neighborhood and stacked together forming a 3D array (groups). The BM3D analysis transform is then applied to the group. The obtained spectral coefficients are manipulated (hard/soft-thresholded) and the collaboratively filtered patches synthesized by the BM3D synthesis transform. This process is repeated over the entire image and the obtained overlapped filtered patches are aggregated in the final image estimate.

The third order High Order Singular Value Decomposition (HOSVD) (see, e.g., [20] - [22]) is adapted for design of 3D complex domain analysis transforms. After applying HOSVD to the 3D groups, we obtain complex-valued group-wise spectrums and three orthonormal complex domain transforms: two for each coordinate of 2D patches and the third one for the longitudinal coordinate of the group. Thus, instead of the fixed real-valued analysis transforms originally proposed in BM3D [19], we obtain group-dependent and data-adaptive complex-valued transforms, where phases and amplitude are linked. This new technique can be understood as a generalization for the complex domain of the BM3D-SAPCA algorithm [23], where Singular Value Decomposition (SVD) is used for design of 2D orthonormal bases for patches, and also of HOSVD-BM3D proposed in [24], where HOSVD is exploited as a generator of 3D/4D real domain orthonormal transforms.

A different approach to complex domain filtering is developed in the recent paper [25] based on the dictionary leaning incorporated in patch-based image restoration. Aiming at optimal sparse representations, and thus at optimal noise removing capabilities, the dictionary is learned from the data that it represents via matrix factorization with sparsity constraints on the code (i.e., the regression coefficients) enforced by the  $l_1$ -norm. Two types of the dictionaries are studied: externally designed from sets of clear images (extra data) and internally designed from noisy data obtained for the image of interest only.

The main goal of this paper is a research and further development of the complex domain BM3D filters which potentially could serve as "plug-and-play priors" applicable for various scenarios with complex domain variables of the

form  $u = ae^{j\varphi}$ .

115 The contribution of this paper concerns the following aspects of the problem:  
(1) Formalization of connections between the complex domain BM3D algorithm and complex domain sparsity; (2) Sparsity optimization and designing a new iterative complex domain BM3D; (3) Extended simulation experiments confirming the state-of-the-art performance of the developed algorithms.

120 In what follows the paper is organized as follows. The observation model and the complex domain BM3D algorithm are presented in Section 2. Links of this algorithm with sparsity modeling is a subject of Section 3. The iterative complex domain BM3D is derived in this section and the convergence proof is given for this algorithm. An extensive experimental study of the complex domain BM3D  
125 and its iterative version is a subject of Section 4. These experiments show that the iterative algorithm enables a better performance and the both algorithms are the state-of-the-art in the field.

## 2. Complex domain BM3D

Let us assume that the observed data  $z : X \rightarrow C$ , where  $X \subset Z^2$  is 2D grid  
130 of size  $\sqrt{n} \times \sqrt{n}$ , are modeled as

$$\begin{aligned} z(x) &= u(x) + \varepsilon(x), \\ u(x) &= a(x)e^{j\varphi(x)}, \end{aligned} \tag{4}$$

where  $x \in X$ ,  $u(x) \in \mathbb{C}^{\sqrt{n} \times \sqrt{n}}$  is a clear complex-valued image, and  $\varepsilon(x) = \varepsilon_I(x) + j\varepsilon_Q(x) \in \mathbb{C}^{\sqrt{n} \times \sqrt{n}}$ , is complex-valued zero-mean Gaussian circular white noise of variance  $\sigma^2$  (i.e.,  $\varepsilon_I$  and  $\varepsilon_Q$  are zero-mean independent Gaussian random variables with variance  $\sigma^2/2$ ).

### 135 2.1. CD-BM3D algorithm

We start from presentation of the complex domain BM3D (CD-BM3D) as it is proposed in [26]. The abbreviation CD-BM3D is introduced in this paper in order to emphasize succession of this algorithm with respect to BM3D.

Following the procedure in patch-based image restoration, the noisy  $\sqrt{n} \times \sqrt{n}$  image  $\mathbf{z} \equiv \{z(x), x \in X\}$  is partitioned into small overlapping rectangular/square patches  $N_1 \times N_2$  defined for each pixel of the image. The basic steps of the algorithm are as follows: grouping, HOSVD transform of 3D groups, hard-thresholding of HOSVD spectrum, inverse HOSVD transform, and aggregation of the overlapping patch estimates. Compared with [19], we have two major differences: a) the images are complex-valued; b) the transform used to carry out 3D filtering is HOSVD, which brings groupwise transform adaptiveness not present in [19]. Similar to [26] these steps can be detailed as follows.

### 1. Grouping

Let  $\mathbf{P}_x \equiv \{z(y), y \in \mathcal{P}_x \subset X\}$  denotes an image patch of size  $N_1 \times N_2$  defined on the domain  $\mathcal{P}_x$ , where the index  $x \in X$  corresponds to the upper-left pixel of the patch. For each  $r$ -th patch (reference patch) we select  $J_r$  similar patches which are closest to the reference patch  $\mathbf{P}_r$ . We define a set  $G_r \subset X$  as

$$G_r \equiv \{x \in X : \underline{b}_r \leq d(\mathbf{P}_x - \mathbf{P}_r)/\sigma^2 \leq \bar{b}_r\}, \quad (5)$$

where  $d(\mathbf{P}_x - \mathbf{P}_r)$  denotes the Euclidean distance between patches  $\mathbf{P}_x$  and  $\mathbf{P}_r$ , and  $\underline{b}_r, \bar{b}_r$  are parameters controlling size of the two-sided confidence interval  $G_r$  testing the hypothesis that  $\mathbf{P}_x$  and  $\mathbf{P}_r$  are noisy versions of underlying close clean patches.

Assuming that the clean patches are identical the distance  $d(\mathbf{P}_x - \mathbf{P}_r)$  has a  $\chi^2(2(N_1 \times N_2))$  distribution. For large  $N_1 N_2$  this  $\chi^2$  distribution is well approximated by Gaussian with mean and variance equal to  $2N_1 N_2 \sigma^2$  and  $4N_1 N_2 \sigma^4$ , respectively. We define the lower and upper bounds in (5) as  $\underline{b}_r = \max(0, 2N_1 N_2 - q_1 2\sqrt{N_1 N_2})$  and  $\bar{b}_r = 2N_1 N_2 + q_1 q_2 2\sqrt{N_1 N_2}$ , where  $q_1$  is a Gaussian distribution quantile. We take  $q_1 = 3$  (three sigma rule) and assume that  $q_2 > 1$  in  $\bar{b}_r$  in order to extend the confidence interval beyond a size obtained under the hypothesis that the clean patches in  $\mathbf{P}_x$  and  $\mathbf{P}_r$  are identical.

The matched noisy patches  $\mathbf{P}_x$ , for  $x \in G_r$  are stacked to form a 3D array of size  $N_1 \times N_2 \times J_r$ , denoted by  $\mathbf{Z}^r$ , where  $J_r$  denotes a length of the array

(the number of elements in  $G_r$ )

165 **2. HOSVD**

The 3D group  $Z^r \subset \mathbb{C}^{N_1 \times N_2 \times J_r}$  can be treated as a tensor of the dimension  $N_1 \times N_2 \times J_r$ . The elements of this tensor can be expressed as  $\mathbf{Z}_{l_1, l_2, l_3}^r$  with  $l_1 = 1, \dots, N_1$ ,  $l_2 = 1, \dots, N_2$  and  $l_3 = 1, \dots, J_r$ . In order to treat the group  $Z^r$  as a whole 3D entity, techniques on the multilinear algebra can be used in order to  
 170 take into account correlations inside and between patches. It is well known that SVD is important for matrix analysis. Similarly, there are a number of various tensor decompositions as the most important ones we mention TUCKER3 and PARAFAC [20] - [22].

In this paper we use the HOSVD (TUCKER3) transform allowing to represent the group-tensor in the form

$$\mathbf{Z}^r = \mathbf{S}^r \times_1 \mathbf{T}_{1,r} \times_2 \mathbf{T}_{2,r} \times_3 \mathbf{T}_{3,r}, \quad (6)$$

where  $\mathbf{T}_{1,r} \subset \mathbb{C}^{N_1 \times N_1}$ ,  $\mathbf{T}_{2,r} \subset \mathbb{C}^{N_2 \times N_2}$  and  $\mathbf{T}_{3,r} \subset \mathbb{C}^{N_{J_r} \times N_{J_r}}$  are orthonormal  
 175 transform matrices,  $\mathbf{S}^r \in \mathbb{C}^{N_1 \times N_2 \times J_r}$  is the so-called *core tensor*, and symbols  $\times_1, \times_2, \times_3$  stand for the products of the corresponding modes (variables). The matrix transform  $\mathbf{T}_{1,r}$  acts with respect to the variable  $l_1$  in  $\mathbf{Z}_{l_1, l_2, l_3}^r$  provided that  $l_2$  and  $l_3$  are fixed, similar meaning have the mode transforms  $\times_2 \mathbf{T}_{2,r}$  and  $\times_3 \mathbf{T}_{3,r}$  with respect to the variables  $l_2$  and  $l_3$ .

180 **3. Thresholding**

In the standard two-dimensional SVD the spectral matrix is diagonal composed from non-negative singular values of the matrix to be analyzed and the transform matrices are real-valued. Usually, a number of large singular values is small and data filtering is produced by zeroing the elements of the diagonal  
 185 spectral matrix which are smaller some threshold. These truncated SVD based approximations have been extensively used in signal and image processing both to carry out denoising and to obtain low rank approximation of the original matrices.

HOSVD applied to the complex-valued data gives the complex-valued orthonormal transform matrices  $\mathbf{T}_{1,r}$ ,  $\mathbf{T}_{2,r}$ ,  $\mathbf{T}_{3,r}$  and a complex-valued core tensor

$\mathbf{S}^r$ . However, as show the experiments, in our tests, a small number of tensor components with large energy (absolute values) dominate the group representation. Thus, assuming that smaller elements of  $\mathbf{S}^r$  are linked to noise and not to essential components of the signal, the element wise thresholding for filtering of  $\mathbf{S}^r$  is used in the form

$$\hat{\mathbf{S}}^r = \text{thresh}(\mathbf{S}^r, \delta_r), \quad (7)$$

where  $\text{thresh}(\cdot)$  stands for the hard-/soft-threshold function.

190 Specific features of the thresholding function for the complex domain are studied in Section 3, where this function is derived as an optimal solution for some optimization problem.

As per rule derived in [27] we select as the universal threshold

$$\delta_r = \eta\sigma\sqrt{2\log N_1 N_2 J_r}, \quad (8)$$

where  $\eta$  parameter of the algorithm is selected from experiments.

After the thresholding the filtered group data are reconstructed using the formula (6) as

$$\hat{\mathbf{U}}^r = \hat{\mathbf{S}}^r \times_1 \mathbf{T}_{1,r} \times_2 \mathbf{T}_{2,r} \times \mathbf{T}_{3,r}. \quad (9)$$

#### 4. Aggregation and wavefield reconstruction

195 After the thresholding step, each of the 3D arrays  $\hat{\mathbf{U}}^r$ , for  $r \in X$ , contains  $J_r$  stacked local patch estimates  $\mathbf{P}_{x \in Q_r}$  of the corresponding true patches.

We remark that due to the patch overlapping and grouping process, the set of patches contained in the 3D groups  $G_r$ , for  $r \in X$ , provides an overcomplete representation of the estimated image  $u$ . Define  $\hat{u}_{r,y}(x)$  as the estimate of  $u(x)$  provided by patch  $y$  if  $y \in G_r$ ,  $x \in \mathcal{P}_y$ , and  $\hat{u}_{r,y}(x) = 0$  otherwise. With these definition in place, we compute the aggregated estimate of  $u(x)$  as the weighted mean

$$\hat{u}(x) = \frac{\sum_{r \in X} g_r \sum_{y \in G_r} \hat{u}_{r,y}(x)}{\sum_{r \in X} g_r \sum_{y \in G_r} \mathcal{I}_{\mathcal{P}_y}(x)}, \quad (10)$$

where  $\mathcal{I}_{\mathcal{P}_y}(x)$  stands for the indicator of set  $\mathcal{P}_y$ .

The weights  $g_r$  are calculated as

$$g_r = 1/\chi(\hat{\mathbf{S}}^r) \quad (11)$$

$\chi(\hat{\mathbf{S}}^r)$  is the cardinality number of  $\hat{\mathbf{S}}^r$ , i.e. the number of active (non-zero) elements of the core tensor  $\hat{\mathbf{S}}^r$  after thresholding.

200 The total power of noise in the core tensor is proportional to the cardinality number. Thus, the weighted mean (10) uses inverse variances for aggregation of multiple estimates.

If we take  $g_r = 1$  for all  $r$ , the denominator of (10) is always greater or equal to 1 because all image pixels are covered at least by a patch. In practice, for 205 most pixels we have  $\sum_{r \in X} \sum_{y \in Q_r} \mathcal{I}_{\mathcal{P}_y}(x) \gg 1$  because a patch containing  $x$  was cooperatively used in many groups.

When  $\hat{u}(x)$  is calculated reconstruction of amplitude and interferometric phase is of the form

$$\hat{a} = \text{abs}(\hat{u}(x)), \hat{\varphi} = \text{arg}(\hat{u}(x)). \quad (12)$$

The input-output relation in this algorithm will be denoted as

$$\hat{u} = \text{CD-BM3D}(z, \delta), \quad (13)$$

where  $\delta$  stands for the thresholding parameter.

## 210 2.2. Overcomplete spectral representations and CD-BM3D

Let  $\mathbf{u} \in \mathbb{C}^n$  be a vectorized representation of the complex-valued object  $u(x)$  in (4). Denote  $\mathbf{a} = \text{abs}(\mathbf{u})$  and  $\boldsymbol{\varphi} = \text{angle}(\mathbf{u}) \in [-\pi, \pi)$  as, respectively, the corresponding images of amplitude (modulus) and interferometric phase,  $\boldsymbol{\varphi}$ . Then we have  $\mathbf{u} = \mathbf{a} \circ \exp(j\boldsymbol{\varphi})$ . In the vectorized representations all functions 215 applied to vectors are to be understood in the component-wise sense; the same applies to multiplications of vectors (denoted as 'o').

With the objective of formulating treatable phase imaging problems, most approaches follow a two-step procedure: in the first step, an estimate of the so-called interferometric (principal, wrapped) phase in the interval  $[-\pi, \pi)$  is

220 determined; in the second step, termed phase unwrapping, the absolute phase  
is inferred by adding of an integer number of  $2\pi$  multiples to the estimated  
interferometric phase [28]. In what follows, we denote the interferometric phase  
as  $\varphi$  and the absolute phase as  $\varphi_{abs}$ . We introduce the phase-wrap operator  $\mathcal{W} :$   
 $\mathbb{R} \mapsto [-\pi, \pi)$ , linking the absolute and interferometric phase as  $\varphi = \mathcal{W}(\varphi_{abs})$ .  
225 We also define the unwrapped phase as  $\varphi_{abs} = \mathcal{W}_1(\varphi)$ . Note that  $\mathcal{W}_1$  is not  
an inverse operator for  $\mathcal{W}$  because the latter is highly non-linear and for  $2D$   
images there is no one-to-one relation between  $\varphi_{abs}$  and  $\varphi$ .

Let us introduce a complex domain sparse representation for  $u(x)$  in the  
form

$$\mathbf{u} = \Psi_{\mathbf{u}}\boldsymbol{\theta}_{\mathbf{u}}, \boldsymbol{\theta}_{\mathbf{u}} = \Phi_{\mathbf{u}}\mathbf{u}, \quad (14)$$

where  $\mathbf{u} \in \mathbb{C}^n$  and  $\boldsymbol{\theta}_{\mathbf{u}} \in \mathbb{C}^p$  are complex-valued object and complex-valued  
object spectrum, respectively.

230 Herein, the syntheses  $\Psi_{\mathbf{u}}$  and analysis  $\Phi_{\mathbf{u}}$  matrices (transforms, dictionaries)  
for  $\mathbf{u}$  are also complex-valued. Following the sparsity rationale it is assumed  
that the spectrum  $\boldsymbol{\theta}_{\mathbf{u}}$  is sparse; i.e., most elements thereof are zero. In order to  
quantify the level of sparsity of  $\boldsymbol{\theta}_{\mathbf{u}}$ , i.e., its number of non-zero (active) elements,  
we use the pseudo  $l_0$ -norm  $\|\cdot\|_0$  defined as a number of non-zero elements of the  
235 vector-argument. Therefore, in the ensuing formulations, we design estimation  
criteria promoting low values of  $\|\boldsymbol{\theta}_{\mathbf{u}}\|_0$ .

Usually, the spectral representations are highly overcomplete with  $p \gg n$ ,  
while the number of the active elements, i.e. the pseudo  $l_0$ -norms of spectra,  
are much smaller than  $p$ .

240 We wish to install a correspondence between sparsity modeling in the form  
(14) and CD-BM3D introduced in Subsection 2.1.

For given BM3D's groups  $\{G_r\}$  and HOSVD transforms  $\{\mathbf{T}_{1,r}, \mathbf{T}_{2,r}, \mathbf{T}_{3,r}\}$   
calculated for all groups the link between the observation  $z(x)$ ,  $x \subset X$ , and  
HOSVD spectra  $\{\mathbf{S}^r\}$  is linear and can be given as

$$\boldsymbol{\theta}_{\mathbf{z}} = \Phi_{\mathbf{z}}\mathbf{z}, \quad (15)$$

where  $\mathbf{z} \in \mathbb{C}^n$  is an observation vector corresponding to (4),  $\boldsymbol{\theta}_{\mathbf{z}} \in \mathbb{C}^p$  is a

vector composed from all items of  $\{\mathbf{S}^r\}$  and the transform matrix  $\Phi_{\mathbf{z}}$  is defined by BM3D grouping and HOSVD operations.

245 Comparing with (14) we may interpret (15) as the analysis transform defined by the steps 1 and 2 of CD-BM3D and applied to the noisy observation.

A synthesis transform, another linear operation in CD-BM3D, is defined by inverse HOSVD and aggregation step 4 of CD-BM3D. This operation can be presented in the form

$$\hat{\mathbf{u}} = \Psi_{\mathbf{z}} \hat{\boldsymbol{\theta}}_{\mathbf{z}}, \quad (16)$$

where  $\hat{\boldsymbol{\theta}}_{\mathbf{z}}$  is a vector of the thresholded (filtered) components of the spectrum  $\boldsymbol{\theta}_{\mathbf{z}}$ ,  $\hat{\mathbf{u}}$  is the vectorized estimate  $\hat{u}(x)$  and  $\Psi_{\mathbf{z}}$  is a synthesis transform matrix.

Therefore, the introduced analysis and synthesis transforms allow to represent CD-BM3D in the compact form:

$$\boldsymbol{\theta}_{\mathbf{z}} = \Phi_{\mathbf{z}} \mathbf{z}, \hat{\boldsymbol{\theta}}_{\mathbf{z}} = \text{thresh}(\boldsymbol{\theta}_{\mathbf{z}}, \delta), \hat{\mathbf{u}} = \Psi_{\mathbf{z}} \hat{\boldsymbol{\theta}}_{\mathbf{z}}. \quad (17)$$

The real domain BM3D as it in [19] is different from CD-BM3D by using 250 the same fixed transforms  $\mathbf{T}_{1,r}$ ,  $\mathbf{T}_{2,r}$ ,  $\mathbf{T}_{3,r}$  for each group. It gives opportunity to go much further in the study of the corresponding sparse representation (14). It is shown in [29] that  $\Phi_{\mathbf{z}}$  and  $\Psi_{\mathbf{z}}$  are non-tight frames (named BM3D frames). Moreover, if  $g_r = 1$ ,  $\Psi_{\mathbf{z}} = \mathbf{W}^{-1} \Phi_{\mathbf{z}}^H$ , where  $\mathbf{W}$  is a diagonal matrix with integers indicating number of groups where the corresponding pixel is used.

255 This statement cannot be extended for CD-BM3D, where the transforms  $\{\mathbf{T}_{1,r}, \mathbf{T}_{2,r}, \mathbf{T}_{3,r}\}$  generated by HOSVD are different for each group. Nevertheless, it can be seen that  $\Psi_{\mathbf{z}} \Phi_{\mathbf{z}} = \mathbf{I}_{n \times n}$  for CD-BM3D. Thus, provided no thresholding,  $\hat{\boldsymbol{\theta}}_{\mathbf{z}} = \boldsymbol{\theta}_{\mathbf{z}}$ , the perfect reconstruction of the input signal is guaranteed,  $\hat{\mathbf{u}} = \Psi_{\mathbf{z}} \Phi_{\mathbf{z}} \mathbf{z} = \mathbf{z}$ .

260 The representation of CD-BM3D in the form (17) is exploited further for derivation of an iterative version of this algorithm. Note, that in implementation of CD-BM3D the transform-matrices  $\Phi_{\mathbf{z}}$  and  $\Psi_{\mathbf{z}}$  are not calculated and passages from  $\mathbf{z}$  to  $\boldsymbol{\theta}_{\mathbf{z}}$  and from  $\hat{\boldsymbol{\theta}}_{\mathbf{z}}$  to  $\hat{\mathbf{u}}$  are defined algorithmically.

### 3. Sparse modeling of complex exponent

#### 265 3.1. Variational formulation

Two different variational formulations classified as the analysis and synthesis approaches can be viewed for sparse modeling. Specifically, in the *synthesis* approach the variational setup for the Gaussian observations (4) is of the form

$$\min_{\boldsymbol{\theta}_{\mathbf{u}}} \|\boldsymbol{\theta}_{\mathbf{u}}\|_p \text{ s.t. } \|\mathbf{z} - \Psi_{\mathbf{u}}\boldsymbol{\theta}_{\mathbf{u}}\|_2^2 < \varepsilon, \quad (18)$$

where  $\Psi_{\mathbf{u}}\boldsymbol{\theta}_{\mathbf{u}}$  means an estimate for  $\mathbf{u}$ ,  $\varepsilon > 0$ , and  $\|\boldsymbol{\theta}_{\mathbf{u}}\|_p$  can be  $\|\boldsymbol{\theta}_{\mathbf{u}}\|_0$  or  $\|\boldsymbol{\theta}_{\mathbf{u}}\|_1$ .

The pseudo-norm  $l_0$ ,  $\|\boldsymbol{\theta}_{\mathbf{u}}\|_0$ , is calculated as a number of nonzero elements of vector  $\boldsymbol{\theta}_{\mathbf{u}}$ . Aiming at optimal sparse representation and thus at optimal noise removing minimization of  $l_0$  is a straightforward idea in sparse modeling. The 270 norm  $l_1$ ,  $\|\boldsymbol{\theta}_{\mathbf{u}}\|_1$ , is a sum of absolute values of elements of vector  $\boldsymbol{\theta}_{\mathbf{u}}$ . In sparse imaging the  $l_1$ -norm is used as a convex replacement for the non-convex  $l_0$  with an intention to reformulate optimization as a convex one.

An elaborated theory and algorithms are strong arguments in favor of con- 275 vexity for optimization. However, on many occasions the solutions given by  $l_0$  and  $l_1$  are close to each other. Both  $l_0$  and  $l_1$  are standard attributes of variational settings supporting sparsity.

The problem (18) is a constrained optimization provided a quadratic norm restriction due to Gaussian random noise in observations.

The alternative *analysis* approach has a different formalization:

$$\min_{\mathbf{u}} \|\Phi_{\mathbf{u}}\mathbf{u}\|_p \text{ s.t. } \|\mathbf{z} - \mathbf{u}\|_2^2 < \varepsilon. \quad (19)$$

280 Here again we minimize the model complexity in the spectral domain provided quadratic restrictions in the image domain. Nevertheless, formal distinctions between these two formulations are quite obvious. In the synthesis approach minimization is produced in the spectral domain and only the synthesis transform  $\Psi_{\mathbf{u}}$  is used. Contrary to it, in the analysis approach minimization 285 is in the image domain and the analysis transform  $\Phi_{\mathbf{u}}$  is used only.

For real-valued domain a comparative study of the analysis and synthesis techniques is a topic of a number of publications and it is well known that the results of optimization can be quite different [30].

Herein, we adopt a different Nash equilibrium formulation. Contrary to the analysis and synthesis approaches it uses both synthesis and analysis transforms and results in a more manageable optimization.

A single criterion constrained optimization in (18)-(19) is replaced by a search for the Nash equilibrium balancing two criteria. Motivations and details of this approach as it is applied to BM3D filtering in the real domain, links with the game theory and demonstration of its efficiency for the sparse inverse imaging can be seen in [29]. In what follows we adapt this Nash equilibrium technique to complex domain.

The maximum likelihood concept for the observations (4) and the sparsity restrictions lead to the criteria:

$$\mathcal{L}_1(\mathbf{u}, \boldsymbol{\theta}_{\mathbf{u}}) = \|\mathbf{z} - \mathbf{u}\|_2^2 + \frac{1}{\gamma} \|\mathbf{u} - \boldsymbol{\Psi}_{\mathbf{u}} \boldsymbol{\theta}_{\mathbf{u}}\|_2^2, \quad (20)$$

$$\mathcal{L}_2(\mathbf{u}, \boldsymbol{\theta}_{\mathbf{u}}) = \tau \cdot \|\boldsymbol{\theta}_{\mathbf{u}}\|_p + \frac{1}{2} \|\boldsymbol{\theta}_{\mathbf{u}} - \boldsymbol{\Phi}_{\mathbf{u}} \mathbf{u}\|_2^2, \quad (21)$$

where  $\gamma > 0$  and  $\tau > 0$  are regularization parameters.

Here  $\boldsymbol{\Psi}_{\mathbf{u}}$ ,  $\boldsymbol{\Phi}_{\mathbf{u}}$  are synthesis and analysis transforms and  $\boldsymbol{\theta}_{\mathbf{u}}$  stands for spectra of the complex-valued  $\mathbf{u}$  as they are introduced above. The first summand in  $\mathcal{L}_1(\mathbf{u}, \boldsymbol{\theta}_{\mathbf{u}})$  corresponds to the minus Gaussian loglikelihood, and the second is a regularization term defined by the differences between the variables  $\mathbf{u}$  and its sparse estimate  $\boldsymbol{\Psi}_{\mathbf{u}} \boldsymbol{\theta}_{\mathbf{u}}$ .

The  $l_p$  in  $\mathcal{L}_2(\boldsymbol{\theta}_{\mathbf{u}})$  promotes the sparsity of  $\mathbf{u}$  in the spectrum domain. The second summand in  $\mathcal{L}_2(\boldsymbol{\theta}_{\mathbf{u}}, \boldsymbol{\theta}_{\mathbf{a}})$  is a quadratic regularization term defined through the difference between the spectrum variable  $\boldsymbol{\theta}_{\mathbf{u}}$  and its analysis estimate  $\boldsymbol{\Phi}_{\mathbf{u}} \mathbf{u}$ .

An equilibrium point  $(\boldsymbol{\theta}_{\mathbf{u}}^*, \mathbf{u}^*)$  for the criteria (20)-(21) can be introduced as

a solution of the following equations:

$$\begin{aligned}\boldsymbol{\theta}_{\mathbf{u}}^* &= \arg \min_{\boldsymbol{\theta}_{\mathbf{u}}} \mathcal{L}_2(\mathbf{u}^*, \boldsymbol{\theta}_{\mathbf{u}}), \\ \mathbf{u}^* &= \arg \min_{\mathbf{u}} \mathcal{L}_1(\mathbf{u}, \boldsymbol{\theta}_{\mathbf{u}}^*).\end{aligned}\tag{22}$$

In terms of game theory this joint balancing of two criteria (20)-(21) leading  
 310 to (22) is interpreted as game of two players identified, respectively, with two  
 variables  $\boldsymbol{\theta}_{\mathbf{u}}$  and  $\mathbf{u}$  and two criteria, respectively,  $\mathcal{L}_2$  and  $\mathcal{L}_1$ . One player is trying  
 to minimize  $\mathcal{L}_2$  by varying only  $\boldsymbol{\theta}_{\mathbf{u}}$ , while another player has as a resource only  
 $\mathbf{u}$  and is trying to minimize  $\mathcal{L}_1$  on  $\mathbf{u}$ . However, the both criteria depend on the  
 both variables. This interaction between the players is called noncooperative if  
 315 the minimization of  $\mathcal{L}_2$  with respect to  $\boldsymbol{\theta}_{\mathbf{u}}$  typically results in an increase in  $\mathcal{L}_1$   
 and the minimization of  $\mathcal{L}_1$  with respect to  $\mathbf{u}$  increases  $\mathcal{L}_2$ . The balance between  
 the variables  $\boldsymbol{\theta}_{\mathbf{u}}^*$  and  $\mathbf{u}^*$  defined in the form (22) means that there is no deviation  
 from  $(\boldsymbol{\theta}_{\mathbf{u}}^*, \mathbf{u}^*)$  such that one of the criteria becomes smaller without increasing  
 the another one. The equilibrium of this game, called Nash equilibrium, is a  
 320 fixed point of the optimization (22).

Following the Nash equilibrium balancing, in general for multiple penalty  
 functions (e.g. [31], [32]), we propose the algorithm composed of alternating  
 iterations minimizing  $\mathcal{L}_1$  and  $\mathcal{L}_2$ .

For the criteria (20)-(21) the Nash equilibrium can be pursued by iterations:

$$\begin{aligned}\boldsymbol{\theta}_{\mathbf{u}}^{t-1} &= \arg \min_{\boldsymbol{\theta}_{\mathbf{u}}} \mathcal{L}_2(\mathbf{u}^{t-1}, \boldsymbol{\theta}_{\mathbf{u}}), \\ \mathbf{u}^t &= \arg \min_{\mathbf{u}} \mathcal{L}_1(\mathbf{u}, \boldsymbol{\theta}_{\mathbf{u}}^{t-1}).\end{aligned}\tag{23}$$

325 In these iterations two players do alternating moves one after another, i.e.  
 $\boldsymbol{\theta}_{\mathbf{u}}^{t-1}$  will be found only when  $\mathbf{u}^{t-1}$  is known and  $\mathbf{u}^t$  is found provided that  $\boldsymbol{\theta}_{\mathbf{u}}^{t-1}$   
 is known.

Minimization of  $\mathcal{L}_1(\mathbf{u}, \mathbf{a})$  which is quadratic on  $\mathbf{u}$  leads to the linear equation  
 $\partial \mathcal{L}_1 / \partial \mathbf{u}^* = 0$  and the solution:

$$\mathbf{u} = (\mathbf{z} + \frac{1}{\gamma} \boldsymbol{\Psi}_{\mathbf{u}} \boldsymbol{\theta}_{\mathbf{u}}) / (1 + \frac{1}{\gamma}).\tag{24}$$

Minimization of  $\mathcal{L}_2$  on  $\boldsymbol{\theta}_{\mathbf{u}}$  results in the complex domain element-wise thresholding of the spectrum  $\Phi_{\mathbf{u}}\mathbf{u}$ : hard-and soft-thresholding, respectively, for optimization with  $l_0$  and  $l_1$ .

The solution of this minimization can be represented in the following form:

$$\hat{\boldsymbol{\theta}}_{\mathbf{u}} = \mathit{thresh}(\Phi_{\mathbf{u}}\mathbf{u}, \delta) \equiv \begin{cases} \Phi_{\mathbf{u}}\mathbf{u} \circ 1[\mathit{abs}(\Phi_{\mathbf{u}}\mathbf{u}) \geq \delta], & \delta = \sqrt{2\tau}, \text{ if } l_p = l_0, \\ \frac{\Phi_{\mathbf{u}}\mathbf{u}}{\mathit{abs}(\Phi_{\mathbf{u}}\mathbf{u})} \circ \max(\mathit{abs}(\Phi_{\mathbf{u}}\mathbf{u}) - \delta, 0), & \delta = \tau, \text{ if } l_p = l_1, \end{cases} \quad (25)$$

where  $1[x] = 1$  if  $x \geq 0$  and  $1[x] = 0$  otherwise.

The thresholding parameter  $\delta$  is equal to  $\sqrt{2\tau}$  for  $l_0$  and equal to  $\tau$  for  $l_1$ . The items of the spectral vectors  $\mathit{abs}(\Phi_{\mathbf{u}}\mathbf{u})$ , which are smaller than  $\delta$  are zeroed in Eq.(25), while the interferometric phase of the complex-valued  $\Phi_{\mathbf{u}}\mathbf{u}$  is preserved for non-zero elements of  $\Phi_{\mathbf{u}}\mathbf{u}$ . Overall, the thresholding manipulates the absolute values only and does not change the phase of the input. Remind that all operations with the vectorized variables are element-wise.

Let us derive the rule (25) from minimization of  $\mathcal{L}_2$  on  $\boldsymbol{\theta}_{\mathbf{u}}$ . First of all note, that the criterion (21) can be rewritten as

$$\mathcal{L}_2(\mathbf{u}, \boldsymbol{\theta}_{\mathbf{u}}) = \tau \cdot \|\mathbf{a}_{\boldsymbol{\theta}_{\mathbf{u}}}\|_p + \frac{1}{2} \|\mathbf{a}_{\boldsymbol{\theta}_{\mathbf{u}}} \circ \exp(j\varphi_{\boldsymbol{\theta}_{\mathbf{u}}}) - \mathbf{a}_{\Phi_{\mathbf{u}}\mathbf{u}} \circ \exp(j\varphi_{\Phi_{\mathbf{u}}\mathbf{u}})\|_2^2, \quad (26)$$

where  $\varphi_{\boldsymbol{\theta}_{\mathbf{u}}}$ ,  $\varphi_{\Phi_{\mathbf{u}}\mathbf{u}}$  are the interferometric phases of  $\boldsymbol{\theta}_{\mathbf{u}}$  and  $\Phi_{\mathbf{u}}\mathbf{u}$ , respectively, and  $\mathbf{a}_{\boldsymbol{\theta}_{\mathbf{u}}}$  and  $\mathbf{a}_{\Phi_{\mathbf{u}}\mathbf{u}}$  are the amplitudes of  $\boldsymbol{\theta}_{\mathbf{u}}$  and  $\Phi_{\mathbf{u}}\mathbf{u}$  in the representation of  $\boldsymbol{\theta}_{\mathbf{u}}$  and  $\Phi_{\mathbf{u}}\mathbf{u}$  in the form  $\boldsymbol{\theta}_{\mathbf{u}} = \mathbf{a}_{\boldsymbol{\theta}_{\mathbf{u}}} \circ \exp(j\varphi_{\boldsymbol{\theta}_{\mathbf{u}}})$ ,  $\Phi_{\mathbf{u}}\mathbf{u} = \mathbf{a}_{\Phi_{\mathbf{u}}\mathbf{u}} \circ \exp(j\varphi_{\Phi_{\mathbf{u}}\mathbf{u}})$ .

Minimization of  $\mathcal{L}_2(\mathbf{u}, \boldsymbol{\theta}_{\mathbf{u}})$  on the complex-valued  $\boldsymbol{\theta}_{\mathbf{u}}$  can be produced independently on amplitude and phase of  $\boldsymbol{\theta}_{\mathbf{u}}$ . Minimization on  $\varphi_{\boldsymbol{\theta}_{\mathbf{u}}}$  for (26) immediately gives

$$\varphi_{\boldsymbol{\theta}_{\mathbf{u}}} = \varphi_{\Phi_{\mathbf{u}}\mathbf{u}}. \quad (27)$$

Inserting this solution in (26) we obtain  $\mathcal{L}_2$  depending only on the amplitudes:

$$\mathcal{L}_2(\mathbf{u}, \boldsymbol{\theta}_{\mathbf{u}})|_{\varphi_{\boldsymbol{\theta}_{\mathbf{u}}} = \varphi_{\Phi_{\mathbf{u}}\mathbf{u}}} = \tau \cdot \|\mathbf{a}_{\boldsymbol{\theta}_{\mathbf{u}}}\|_p + \frac{1}{2} \|\mathbf{a}_{\boldsymbol{\theta}_{\mathbf{u}}} - \mathbf{a}_{\Phi_{\mathbf{u}}\mathbf{u}}\|_2^2. \quad (28)$$

It can be verified that minimization of  $\mathcal{L}_2(\mathbf{u}, \boldsymbol{\theta}_{\mathbf{u}})|_{\varphi_{\boldsymbol{\theta}_{\mathbf{u}}} = \varphi_{\boldsymbol{\Phi}_{\mathbf{u}}\mathbf{u}}}$  on real-valued  $\mathbf{a}_{\boldsymbol{\theta}_{\mathbf{u}}}$  gives the standard hard- and soft-thresholding functions:

$$a_{out} = f(a_{in}, \delta) \equiv \begin{cases} a_{in} \times 1[|a_{in}| \geq \sqrt{2\tau}], & \text{if } l_p = l_0, \\ \text{sign}(a_{in}) \times \max(|a_{in}| - \tau, 0), & \text{if } l_p = l_1, \end{cases} \quad (29)$$

where  $a_{in}$  and  $a_{out}$  are elements of the amplitude vectors  $\mathbf{a}_{\boldsymbol{\Phi}_{\mathbf{u}}\mathbf{u}}$  and  $\mathbf{a}_{\boldsymbol{\theta}_{\mathbf{u}}}$ , respectively.

For the complex valued  $x_{in} = a_{in} \exp(j\varphi_{in})$  and  $x_{out} = a_{out} \exp(j\varphi_{out})$  due to (27)  $\varphi_{in} = \varphi_{out}$  and we obtain from (29)

$$x_{out} = \text{thresh}(x_{in}, \delta) \equiv \begin{cases} x_{in} \times 1[\text{abs}(x_{in}) \geq \sqrt{2\tau}], & \text{if } l_p = l_0, \\ \frac{x_{in}}{\text{abs}(x_{in})} \times \max(\text{abs}(x_{in}) - \tau, 0), & \text{if } l_p = l_1, \end{cases}, \quad (30)$$

where  $x_{in}$  and  $x_{out}$  are elements of the complex-valued vectors  $\boldsymbol{\Phi}_{\mathbf{u}}\mathbf{u}$  and  $\boldsymbol{\theta}_{\mathbf{u}}$ , respectively. 345

It is useful to note here that in representation of complex-valued  $x$  in the form  $x = a_x \exp(j\varphi_x)$  the amplitude  $a_x$  may take positive and negative values. Contrary to it in the representation  $x = \text{abs}(x) \exp(j\tilde{\varphi}_x)$  the amplitude  $\text{abs}(x) \geq 0$  and the sign of  $a_x$  is translated in the phase  $\tilde{\varphi}_x$  by including summand  $\pi$  if  $a_x < 0$ . In the derivation of (30) we use  $a_{x_{in}}/\text{sign}(a_{x_{in}}) = \text{abs}(a_{x_{in}}) = \text{abs}(x_{in})$ . 350

The formula (25) to be proved is a vectorized version of (30) applied to a vectorial input.

### 3.2. Iterative CD-BM3D

Let us use CD-BM3D transforms as the analysis and synthesis operators for iterations (23). These analysis and synthesis transforms are complex-valued obtained through HOSVD applied to non-local BM3D groups. 355

It follows from (17) that  $\boldsymbol{\Psi}_{\mathbf{u}}\boldsymbol{\theta}_{\mathbf{u}}$ , where  $\boldsymbol{\theta}_{\mathbf{u}} = \text{thresh}(\boldsymbol{\Phi}_{\mathbf{u}}\mathbf{u}, \delta)$ , is the output of the CD-BM3D filter for the input  $\mathbf{u}$ , provided a given grouping. The estimates

Table 1: ITERATIVE CD-BM3D.

	<b>Input:</b> $z \in \mathbb{C}^{\sqrt{n} \times \sqrt{n}}$ (noisy data set)
	Parameters: $\alpha > 0$ (regularization),
	$\delta > 0$ (thresholding),
	$K$ (iteration number).
	Initialization: $u^0 = z$ ;
	<b>Output:</b> $\hat{u} \in \mathbb{C}^{\sqrt{n} \times \sqrt{n}}$ ;
1:	for $t = 1, \dots, K$
2:	$v^t = u^{t-1} + \alpha(z - u^{t-1})$ ;
3:	$u^t = CD\text{-}BM3D(v^t, \delta)$ ;
4:	<i>end</i>
	$\hat{u} = u^K$ .

of  $\mathbf{u}$  and  $\boldsymbol{\theta}_{\mathbf{u}}$  are calculated according to (24)-(25). Using these estimates in the  
360 iterations (23) we arrive to the algorithm shown in Table I.

In Table I all variables are shown for 2D complex domain  $\mathbb{C}^2$ , what makes the formulas simpler and different from those in (24)-(25), where the estimates are presented in the vectorized form.

In this presentation of the algorithm we replace the parameter  $\gamma$  by  $\alpha =$   
365  $1/(1 + 1/\gamma)$ ,  $0 < \alpha < 1$  for  $\gamma > 0$ .

It is not difficult to realize that for any  $\alpha$  the first iteration of this algorithm gives  $u^1 = CD\text{-}BM3D(z, \delta)$  as an output of the CD-BM3D algorithm with the observation  $z$  as the input.

According to Step 2 the estimate update is calculated as the sum of the  
370 previous estimate and the deviation of this estimate from the observation  $z$ . The step size  $\alpha$  defines a magnitude of observation noise in the update. This update is filtered at Step 3 of the algorithm.

The free parameters of this algorithm are  $\alpha$  and  $\delta$ . It is typical to use the algorithms derived from the variation formulation similar to (20)-(21) with  
375 varying parameter  $\alpha_t, \delta_t$ , such that  $\alpha_t, \delta_t \rightarrow 0$ .

### 3.3. Convergence of iterative CD-BM3D

The iterative CD-BM3D (Table I) can be rewritten as a single line

$$u^t = CD\text{-}BM3D(u^{t-1} + \alpha(z - u^{t-1}), \delta). \quad (31)$$

A fixed or steady-state point  $\tilde{u}$  of the algorithm is a solution of the equation

$$\tilde{u} = CD\text{-}BM3D(\tilde{u} + \alpha(z - \tilde{u}), \delta). \quad (32)$$

The asymptotic analysis of the proposed iterative algorithm concerns the convergence of the iterations (31) to the steady-state solution (32) when the iteration number increases. We show the uniqueness of the steady-state solution and prove the convergence provided that the filter *CD-BM3D* is a nonexpensive operator satisfying the Lipschitz condition. Provided this assumption the proof is quite routine following the standard techniques in the field (e.g. [33]).  
380 However, the operator *CD-BM3D* is non-linear and it is not possible to check the Lipschitz condition analytically. Instead we exploit an simulation study of the algorithm which confirms that the Lipschitz inequality is fulfilled for *CD-BM3D*.  
385 Thus, overall the convergence proof is semi-heuristic based on the assumption that the Lipschitz condition holds what is confirmed by computational experiments. In the demo software publicly available for the proposed algorithm there are routines checking the Lipschitz property for CD-BM3D.

390 **Proposition 1.** *Let CD-BM3D be a nonexpansive operator satisfying the Lipschitz condition:*

$$\begin{aligned} \|u^1 - u^2\|_F &\leq k_\delta \|z^1 - z^2\|_F, \quad z^1, z^2 \in \mathbb{C}^{\sqrt{n} \times \sqrt{n}}, \\ 0 &\leq k_\delta \leq 1, \end{aligned} \quad (33)$$

where  $u^1 = CD\text{-}BM3D(z^1, \delta)$ ,  $u^2 = CD\text{-}BM3D(z^2, \delta)$  and  $\|\cdot\|_F$  stands for the Frobenius norm.

395 Then, the fixed-point equation (32) has a uniqueness solution and the iterative CD-BM3D algorithm converges to this solution with a geometric convergence

rate

$$\begin{aligned} \|u^t - \tilde{u}\|_F &\leq q \|u^{t-1} - \tilde{u}\|_F, \\ q &= (1 - \alpha)k_\delta < 1. \end{aligned} \tag{34}$$

**Proof.** Let us assume that there are two different solutions of (32)  $\tilde{u}^1$  and  $\tilde{u}^2$ . For the difference of these solutions we obtain due to (32) and (33)

$$\begin{aligned} \|\tilde{u}^1 - \tilde{u}^2\|_F &= \|CD\text{-}BM3D(\tilde{u}^1 + \alpha(z - \tilde{u}^1), \delta) - \\ &CD\text{-}BM3D(\tilde{u}^2 + \alpha(z - \tilde{u}^2), \delta)\|_F \leq \\ &q \|\tilde{u}^1 - \tilde{u}^2\|_F. \end{aligned} \tag{35}$$

Iterations of the last inequality show that  $\|\tilde{u}^1 - \tilde{u}^2\|_F \leq q^k \|\tilde{u}^1 - \tilde{u}^2\|_F$ , for  
 400 any integer  $k > 0$ . Then,  $\|\tilde{u}^1 - \tilde{u}^2\|_F \rightarrow 0$  as  $k \rightarrow \infty$ , i.e. there are no two  
 different solutions. It proves by contradiction the uniqueness of the fixed-point  
 solution.

Further, consider difference between  $u^t$  and  $\tilde{u}$ . Calculations similar to (35)  
 show that  $\|u^t - \tilde{u}\|_F \leq q \|u^{t-1} - \tilde{u}\|_F$ . By contradiction, it proves (34) and  
 405 defines the convergence rate parameter  $q$ . ■

It is obvious from the proof that actually the proposition is a consequence  
 of the Lipschitz condition (33). The algorithm CD-BM3D has a sophisticated  
 nonlinear structure with an imbedded combinatorial patch-wise grouping and  
 data dependent HOSVD transforms different for each group. Thus, it is hard to  
 410 expect that the Lipschitz condition can be proved for this type of the algorithms.

We treat the Lipschitz condition (33) as a fruitful conjecture and validated it  
 empirically by extensive experimental study produced for various types of input  
 complex domain images and different parameters of CD-BM3D.

The following four scenarios of these experiments should be mentioned.

415 I). The input complex exponents are random  $z^1 = |a_1(x)|e^{j\varphi_1(x)}$  and  $z^2 =$   
 $|a_2(x)|e^{j\varphi_2(x)}$ , where  $a_1(x)$ ,  $a_2(x)$ ,  $\varphi_1(x)$  and  $\varphi_2(x)$  are zero-mean  $2D$  Gaussian.  
 We considered these random amplitudes and phases with correlation on  $x$  vary-  
 ing from i.i.d. to strongly correlated ones. This correlation was enforced by  $2D$

convolution of the i.i.d. Gaussian random  $a_1(x)$ ,  $a_2(x)$ ,  $\varphi_1(x)$  and  $\varphi_2(x)$  with  
420 uniform smoothing kernels of different width.

The Lipschitz parameter  $k_\delta$  is calculated as

$$k_\delta = \|u^1 - u^2\|_F / \|z^1 - z^2\|_F. \quad (36)$$

For all experiments and for various threshold parameters of CD-BM3D the results for (36) confirm that  $k_\delta \leq 1$ .

2). The input signals  $z^1$  and  $z^2$  are noisy object images  $u^1$  and  $u^2$ , respectively, with the object complex exponents used in our experiments in Section  
425 4.2.1.

In Figs.1 and 2 we show the estimates of the Lipschitz parameter  $k_\delta$  obtained for the five test-images from Section 4.2.1 provided that  $u^1 = u^2$  and  $\sigma = .1$  and  $\sigma = .9$ . In these figures each curves corresponds to one of the test-images. We do not specify relations between the curves and the test-images as only a qualitative behavior of the curves is of the interest.

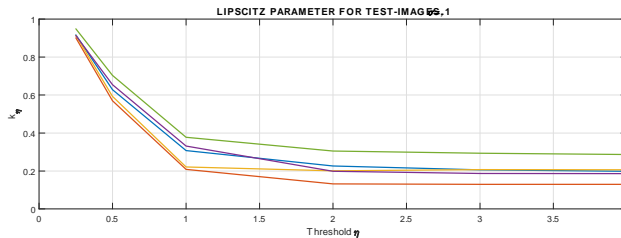


Figure 1: The estimates of the Lipschitz parameter as a function of the threshold parameter  $\eta$  in (8),  $\sigma = .1$ .

430

In these images  $k_\delta$  is given versus the threshold parameter  $\eta$  in (8). First, all  $k_\delta < 1$  and they are monotonically decreasing up to some limits as the threshold grows. The behavior of the curves is quite similar for  $\sigma = .1$  and  $\sigma = .9$ .

3) Let in the scenario 2) the objects  $u^1$  and  $u^2$  be different in any pair-wise  
435 combination of the tested five images. Then, for the high level noise,  $\sigma = 0.9$ ,  $k_\delta \leq 1$  and close to 1, for various threshold values.

For the lower value of  $\sigma$ ,  $\sigma = 0.1$ ,  $k_\delta < 1$  and it is decreasing for larger thresholds. However, this decreasing is much slower than it is in Figs.1-2.

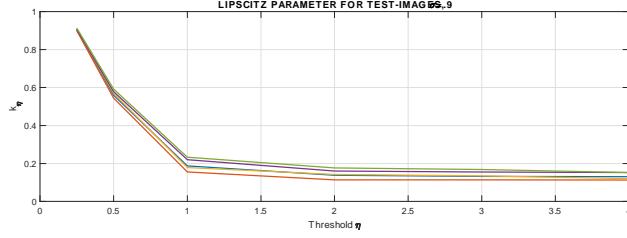


Figure 2: The estimates of the Lipschitz parameter as a function of the threshold parameter  $\eta$  in (8),  $\sigma = .9$ .

4) In this scenario one of the input signals is  $u^t$  defined by the algorithm iterations and the second one is the fixed point  $\tilde{u}$  of these iterations. The Lipschitz parameter is estimated as

$$k_{\delta}^t = \|CD-BM3D(\tilde{u}, \delta) - CD-BM3D(u^t, \delta)\|_F / \|\tilde{u} - u^t\|_F. \quad (37)$$

In this case we calculate the estimates  $k_{\delta}^t$  varying in iterations  $t$  and defined  
 440 on the trajectories of the algorithm's iterations. The examples of this kind of  
 curves for  $k_{\delta}^t$  are shown in Fig.3. These curves are obtained for the truncated  
 Gaussian phase test-image (Section 4.2.1) and a set of noise variances  $\sigma^2$ .

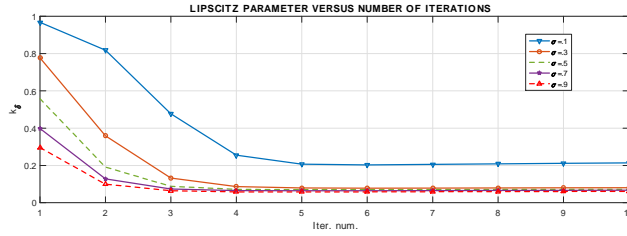


Figure 3: The estimates of the Lipschitz parameter calculated on trajectories of the iterative CD-BM3D.

We may conclude that  $k_{\delta}^t < 1$ . Lower  $\sigma^2$  results in uniformly higher values  
 of  $k_{\delta}^t$ . In iterations,  $k_{\delta}^t$  are decreasing as  $t$  grows and converge to some invariant  
 445 values. These results demonstrate that the convergence rate as defined in (34)  
 is improving in iterations as  $t \rightarrow \infty$ .

The curves in Figs.1-3 are obtained for CD-BM3D equipped with the hard-

thresholding for filtering. Experiments produced for CD-BM3D with the soft-thresholding systematically show low values for the Lipschitz parameter.

#### 450 4. Simulation experiments

In this section, we present simulation results illustrating effectiveness of the developed CD-BM3D algorithms in the basic and iterative versions. Based on the true interferometric phase  $\varphi$  and on the interferometric phase estimate  $\hat{\varphi} = \text{angle}(\hat{u})$  we define the peak signal-to-noise ratio (PSNR) for the phase as

$$PSNR_{\varphi} = 10 \log_{10} \frac{4n\pi^2}{\|\mathcal{W}(\hat{\varphi} - \varphi)\|_F^2} [dB], \quad (38)$$

where  $n$  is the image size and the wrapping operator  $\mathcal{W}$  is used in order to eliminate the phase-shift error multiple to  $2\pi$ .

We unwrap the estimated interferometric phase with the PUMA algorithm [35] in order to get estimates of the true absolute phase  $\varphi_{abs}$ . The accuracy for the absolute phase reconstruction is evaluated by root-mean-square-error (RMSE):

$$RMSE_{\varphi_{abs}} = \sqrt{\frac{1}{n} \|(\hat{\varphi}_{abs} - \varphi_{abs} - \Delta_{\varphi})\|_F^2}, \quad (39)$$

where a scalar  $\Delta_{\varphi}$  compensates a invariant shift in the absolute phase estimation due to the estimation procedure. This  $\Delta_{\varphi}$  is calculated as the mean of the difference  $\hat{\varphi}_{abs} - \varphi_{abs}$ .

The reconstruction accuracy for the true amplitude  $a$  is characterized by *PSNR*:

$$PSNR_{ampl} = 10 \log_{10} \frac{n \max^2(a)}{\|a - \hat{a}\|_F^2} [dB], \quad (40)$$

where  $\hat{a} = \text{abs}(\hat{u})$  is an estimate of amplitude.

In our experiments a comparison of the hard-thresholding versus the soft-thresholding in CD-BM3D is definitely in favor of the hard-thresholding. It is why all results demonstrated in this section are obtained by CD-BM3D with the hard-thresholding.

The developed CD-BM3Ds are compared with the SpInPhase algorithm [25] and Window Fourier Transform (WFT) [?, [34]. The author's codes of these

algorithms are publicly available <sup>1,2</sup>. The SpInPhase algorithm is applied in the internal dictionary learning mode using for estimation only noisy data in order to have a fair comparison versus the CD-BM3Ds. In WFT the windowed  
465 Fourier transform of  $z$  is calculated and hard thresholded. The inverse windowed Fourier transform is applied in order to obtain the estimates of  $\varphi$  and  $a$ . The WFT estimates were obtained with the following parameters: size of the windows  $\sigma_x = \sigma_y = 4$ ; threshold for the windowed Fourier transform  $th = 3\sigma$ ;  
470 frequency interval  $[-\pi, \pi]$ ; and sampling interval 0.1. This setting was determined experimentally in [25] aiming at optimal performance for the set of the phase test images considered in Subsection 4.2.1. Remark that this setting yields considerable better results than that recommended in [?] (i.e.,  $\sigma_x = \sigma_y = 4$  and  $[-\pi/2, \pi/2]$ ). We use SpInPhase and WFT for comparison as the  
475 current state-of-the-art for the interferometric phase reconstruction. Both these algorithms operate in complex domain.

In our MATLAB implementation of CD-BM3Ds we use the tool box *tp-tool090831* for HOSVD transform <sup>3</sup> and the PUMA algorithm for phase unwrapping [35]<sup>4</sup>.

480 The simulation experiments are produced on a personal computer: Intel Core i7-4800 CPU@2.70 GHz and 32.00 GB RAM. All results presented in this section can be reproduced by running the publicly available MATLAB demo-codes including also the codes of the SpInPhase and WFT algorithms <sup>5</sup>.

#### 4.1. Parameters of CD-BM3D algorithms

485 We use two groups of test-images for phase: 1) piece-wise smooth absolute phase and 2) "natural" images (cameraman, Lena) with intrinsic geometrical structures. For the first group we reconstruct both interferometric and absolute phase while for the second group we reconstruct interferometric phase only. The

---

<sup>1</sup><http://www.lx.it.pt/~bioucas/publications.html>

<sup>2</sup>WFT-WFT-<http://www.mathworks.fr/matlabcentral/fileexchange/24892>

<sup>3</sup>tpool-090831- <http://www.tp-control.hu/index.php/About>

<sup>4</sup>PUMA-<http://www.lx.it.pt/~bioucas/code.htm>

<sup>5</sup><http://www.cs.tut.fi/~lasip/DDT/index3.html>

second group of images is too complex for existing phase unwrapping algorithms  
 490 and, practically, the unwrapping for this type of images is impossible even for  
 noiseless data. Thus, only the wrapped phase can be reconstructed for "natural"  
 images. In our modeling in order to preserve these test-images from disruption  
 by wrapping in observation (4) we scaled phase to the interval  $[0, \pi/4]$  radians.

For the parameters of CD-BM3D defining the grouping we follow the con-  
 495 ventional setup of the standard BM3D: the patch size  $8 \times 8$ , the maximum group  
 length is bounded by 32 and the step size between the groups is equal to 3.

Some parameters of the algorithms are different for the two groups of im-  
 ages. In experiments with the first group of the test-images: for CD-BM3D,  
 the threshold parameter  $\eta = 1.8$ , with exclusion  $\eta = 2.7$  for  $\sigma = 0.1$ , and for  
 500 iterative CD-BM3D,  $\eta = 1$ , with exclusion  $\eta = 2$  for  $\sigma = 0.1$ , and  $\alpha = 0.6$  for  
 $\sigma < 0.5$  and  $\alpha = 0.56$  for  $\sigma \geq 0.5$ . Remind that the parameter  $\eta$  is linked with  
 the threshold  $\delta$  according to (8).

For the second group of the test-images CD-BM3D is used with the threshold  
 parameter  $\eta = 1.1$ . In iterative CD-BM3D the parameters  $\eta$  and  $\alpha$  are varying  
 505 in iterations according to the rule  $\eta^t = \mu\eta^{t-1}$  and  $\alpha^t = \mu\alpha^{t-1}$ , where  $\eta^0 = 0.7$ ,  
 $\alpha^0 = 0.65$  and  $\mu = 0.98$ . With these parameters 5 iterations of this algorithm  
 suffice the convergence. In what follows the iteration number is always equal to  
 5.

## 4.2. Performance evaluation

### 510 4.2.1. Piece-wise smooth absolute phase images

The results are given for the observation model (4) with the following set  
 of the absolute phase images: truncated Gaussian, shear plane, sinusoidal con-  
 tinuous, sinusoidal discontinuous, mountains (for these surfaces see Fig.5). The  
 amplitude  $a(x) = 1$ .

515 The true, noisy and iterative CD-BM3D interferometric phase images are  
 demonstrated in Fig.4. The noisy data and reconstructions are given for the  
 high level of the additive noise with  $\sigma = 0.9$ . It is clear from the middle row of  
 these images that the degradation of the interferometric phase due to the noise

is very strong. Nevertheless, the reconstructions (last row in Fig.4) show quite  
 520 clear images close to the true ones.

The corresponding absolute phases (true and reconstructions) can be seen  
 in Fig.5. Each small double-image shows both the true (left) and reconstructed  
 absolute phase (right). The degradation of reconstruction due to the noise is  
 well seen in the truncated Gaussian and nearly invisible for other test-images.

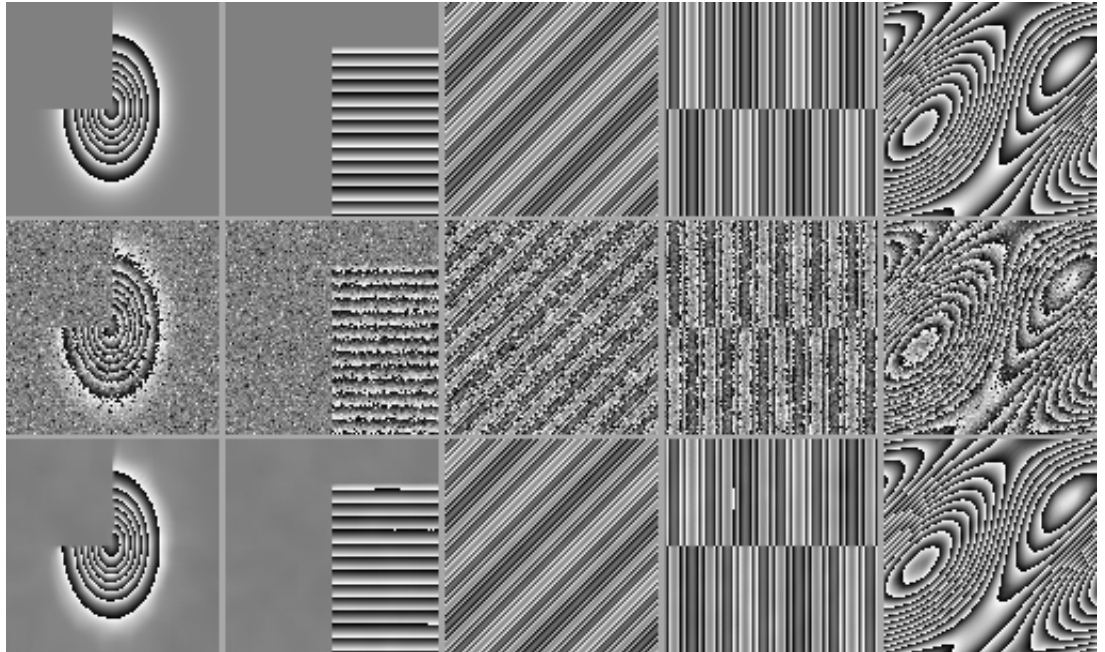
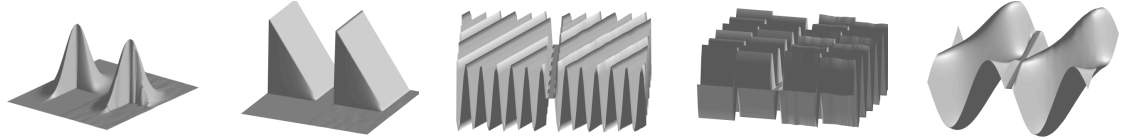


Figure 4: (From left to right) Truncated Gaussian, shear planes, continuous sinusoidal, discontinuous sinusoidal, mountains. (From top to bottom) True, noisy ( $\sigma = 0.9$ ) and interferometric phase images reconstructed by iterative CD-BM3D.

525 The accuracy of reconstruction is detailed in Table 2. Here we can see the  
 columns:  $\text{PSNR}_\varphi$  for interferometric phase,  $\text{RMSE}_{\varphi_{abs}}$  for absolute phase and  
 $\text{PSNR}_{ampl}$  for amplitude. These results are shown for five values of  $\sigma$  varying  
 from the nearly noiseless data ( $\sigma = .1$ ) to very difficult reconstructions from the  
 high level noise observations with  $\sigma = 0.9$ . The following notation is used for  
 530 the algorithms in this table.  $\text{BM}_1$  and  $\text{BM}_2$  stand for CD-BM3D and iterative

Figure 5: Absolute phase surfaces: (from left to right) truncated Gaussian, shear planes, continuous sinusoidal, discontinuous sinusoidal, mountains. In each small image we show the true surface (left) and the iterative CD-BM3D reconstruction (right).



CD-BM3D, respectively. Sp denotes the SpInPhase algorithm, and WFT stands for the WFT algorithm. The column *Surf* indicates phase test-image. The best results are marked in bold which are for the interferometric phase reconstruction (column  $\text{PSNR}_{\varphi}$ ) are always in  $\text{BM}_2$  columns.

535 The comparison of CD-BM3D versus iterative CD-BM3D shows to what extent the iterations improve CD-BM3D. The interferometric phase reconstruction is of special interest (column  $\text{PSNR}_{\varphi}$ ). For the truncated Gaussian phase the advantage of  $\text{BM}_2$  is clear for  $\sigma < 0.9$  with a PSNR improvement about 0.6 dB. For  $\sigma = 0.9$  the accuracy of  $\text{BM}_1$  and  $\text{BM}_2$  are identical. Comparison of  
 540 these algorithm with respect to both Sp and WFT is definitely in favor of  $\text{BM}_1$  and  $\text{BM}_2$ .

For other phase test-images the advantage of  $\text{BM}_2$  with respect to  $\text{BM}_1$  is even more definite. The strongest improvement 1.3 – 2.4 dB is demonstrated for the sinusoidal continuous phase. For the share planes the improvement is  
 545 varying from 1 dB to 2.7 dB. For the sinusoidal discontinues and mountains the improvement in  $\text{PSNR}_{\varphi}$  is from 0.4 dB to 1.1 dB. The comparison with respect to Sp and WFT is always in favor of the CD-BM3D algorithms.

Comparison of  $\text{RMSE}_{\varphi_{abs}}$  and  $\text{PSNR}_{ampl}$  gives similar but not identical conclusions again mainly in favor of both  $\text{BM}_1$  and  $\text{BM}_2$ , while sometime best  
 550 results are demonstrated by Sp. Note that the parameters of Sp and WFT for this set of test-images are optimized in [25].

The test-images in this section are characterized by piece-wise smooth absolute phase surfaces of a large variation range (from 10 to 90 radians) leading

to quite complex fringe patterns for wrapped phases. A direct application to  
555 these noisy fringes the standard strong denoisers, for instance the BM3D fil-  
ter, is not successful (e.g. [34], [36]). The state-of-the-art performance of the  
algorithms compared in this section are mainly due to their functioning in the  
complex domain.

#### 4.2.2. Natural images

560 Cameraman and Lena images ( $256 \times 256$ ) typical for image processing studies  
are used in these tests. For phase modeling these images are scaled to the interval  
[0  $\pi/4$ ] in order to avoid problems caused by phase wrapping and unwrapping.  
The goal of these tests is to evaluate how good are the developed algorithms for  
phase images of complex geometrical structure full of small details.

565 The results shown in Table 3 are in favor of iterative CD-BM3D (BM<sub>2</sub>) for  
the phase reconstruction and in favor of SpInPhase for the amplitude recon-  
struction. Comparing CDBM3D versus iterative CDBM3D we may note that  
the improvement in phase imaging due to the iterations is about 0.7 dB. How-  
ever, for the amplitude reconstruction on many occasions CDBM3D preforms  
570 better than iterative CDBM3D with the advantage about 0.6 dB.

Phase imaging achieved by iterative CDBM3D is illustrated for  $128 \times 128$   
fragments of the test-images in Figs.6-7. For comparison we show also the  
phase images of the noisy complex-valued observations. The input data of the  
algorithm are quite noisy and the reconstructed images are of quite a good  
575 quality. The improvement due to this processing in *PSNR* is about 10 dB.

Further, we consider different type experiments. Let us assume that both  
phase and amplitude are spatially varying and varying in different ways. In  
these tests cameraman is used as a phase and Lena as an amplitude. The phase  
is scaled to the interval [0  $\pi/4$ ] and the amplitude to the interval [0.1 1.1]. The  
580 latter is done in order to avoid zero or close to zero values for amplitude.

Figs.8 and 9 show the results obtained for the noiseless and small level noise  
( $\sigma = 0.1$ ) scenarios. The columns in these images from left-to-right correspond  
to the BM<sub>2</sub>, Sp and WFT algorithms. In the noiseless case the phase recon-

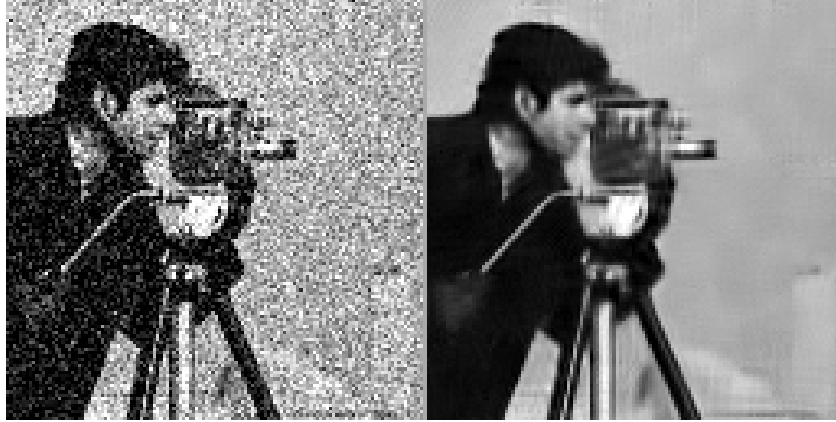


Figure 6: Cameraman phase images: noisy phase observation (left) and iterative CDBM3D phase reconstruction (right),  $\sigma = 0.3$ . PSNR for the reconstruction is  $39.56 \text{ dB}$  and for the noisy phase is  $29.22 \text{ dB}$ .

struction is quite successful for all algorithms. Nevertheless the best result are  
 585 by  $\text{BM}_2$ : Sp produces an oversmoothed imaging and details given by WFT are not so clean and sharp as those in  $\text{BM}_2$  imaging.

The amplitude reconstruction (Lena) is not so good. In particular, we may note traces of the phase cameraman profile on Lena's hat. In the most obvious form it is seen in the Sp image.

590 Noisy data in this scenario with Lena for phase and cameraman for amplitude result in a serious degradation of both phase and amplitude reconstructions (Fig.9). The Sp phase image is again oversmoothed but visually it is even better than the corresponding Sp phase image for the noiseless case. Both phase reconstructions for  $\text{BM}_2$  and WFT are damaged by strong artifacts, while  $\text{BM}_2$   
 595 looks better. For the amplitude reconstruction again visual quality is better for  $\text{BM}_2$  as compared with Sp and WFT.



Figure 7: Lena phase images: noisy phase observation (left) and iterative CDBM3D phase reconstruction (right),  $\sigma = 0.3$ . PSNR for the reconstruction is 40.29 dB and for the noisy phase is 29.27 dB.

In the following more sophisticated tests we assume that the phase is a sum of two terms: cameraman as it is in the previous test and a quadratic phase. This quadratic phase component is typical for coherent optics experiments. It imitates effects of a spherical wave impinging on the phase object. In this case the absolute phase in the model (4) is of the form  $\varphi_{abs} = \varphi_{quad} + \varphi_o$ , where  $\varphi_o$  stands for the object phase (cameraman) and  $\varphi_{quad}$  is the quadratic phase term. The wrapped phase of the observed  $z$  is shown in Fig.10, where the circular fringes appear due to  $\varphi_{quad}$  of the range upto 20 radians. The features of the cameraman can be recognized as a background (or foreground) of these fringes. The noise effects are clearly seen in these phase images. Iterative CD-BM3D was used for the phase reconstruction. After unwrapping this reconstruction gives an absolute estimate  $\hat{\varphi}_{abs}$ . The range of the object phase equal to  $\pi/4$  is much smaller than 20 radian variations of  $\varphi_{quad}$ . In order to make visible the object phase reconstruction we show in Fig.11 a difference  $\hat{\varphi}_{abs} - \varphi_{quad}$  as an estimate of  $\varphi_o$ . The quality achieved for the object phase reconstruction is quite good naturally degrading as soon as the noise standard deviation becomes larger.



Figure 8: Reconstruction of varying phase (cameraman) and amplitude (Lena): from left-to-right:  $\text{BM}_2$ , Sp, WFT algorithms, noiseless observations,  $\sigma = 0$ .

615 *4.2.3. Computational complexity*

The theoretical complexity analysis produced in [24] for real domain BM3D with incorporated HOSVD for basis design is completely applicable to CDBM3D. In particular, it is shown that provided fixed parameters of the algorithm the computational time is proportional to the image size. One can see also in [24]  
 620 the asymptotic for influence of the patch size and group length on the computational time.

We are focussed on a different task: experimental comparative analysis of the algorithms tested in this section. In all experiments we use the same complex-valued image rescaled to different sizes. Lena is selected as a test-image for the  
 625 phase and the amplitude is invariant equal to 1.

In Table 4 we show the mean values of the computational time obtained for different size images. The averaging is done over the computational times



Figure 9: Reconstruction of varying phase (cameraman) and amplitude (Lena): from left-to-right:  $BM_2$ ,  $Sp$ ,  $WFT$  algorithms, noisy observations,  $\sigma = 0.1$ .

calculated for  $\sigma = [0.1, 0.3, 0.5, 0.7, 0.9]$ . For the smallest size image,  $100 \times 100$ ,  $BM_1$  is the fastest algorithm: twice faster than  $WFT$  and about 20 times faster  
630 than  $Sp$ . For larger size images the computational time of  $BM_1$  and  $WFT$  is nearly equal and  $BM_2$  is the slowest algorithm.

Note that the computations time for  $BM_1$  is about proportional to the image size, what is in agreement with the asymptotic result in [24].

Further analysis was done in order to know how the computational time  
635 of  $BM_1$  is distributed between  $BM3D$  and  $HOSVD$  operations. This time sharing is more or less the same for all image sizes. Roughly speaking, it is about 70% for  $BM3D$  and about 25% for  $HOSVD$ .

#### 4.3. Sparsity of $CD$ - $BM3D$ modeling

The complex domain sparsity implemented in  $CD$ - $BM3D$  algorithms is dis-  
640 cussed in this section.

Remind that for each reference pixel we build a  $3D$  array (group) and apply

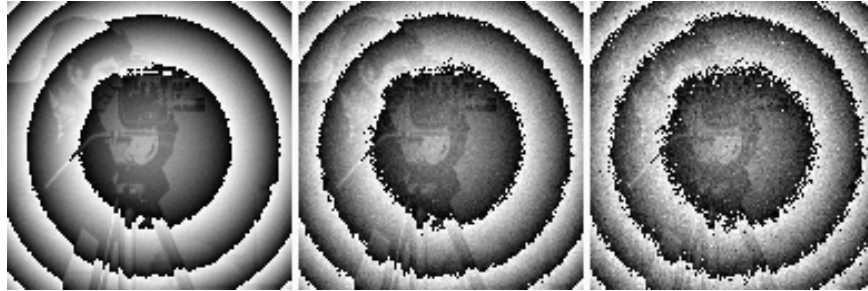


Figure 10: Noisy observation phase. From left to right  $\sigma = 0.1$ ,  $\sigma = 0.3$ ,  $\sigma = 0.5$ .



Figure 11: Reconstruction of absolute phase minus quadratic background phase, iterative CD-BM3D algorithm. From left to right  $\sigma = 0.1$ ,  $\sigma = 0.3$ ,  $\sigma = 0.5$ .

HOSVD in order to get the corresponding  $3D$  core array (complex domain spectrum). The maximal number of items in the  $3D$  group core-tensor is  $8 \times 8 \times 32 = 2048$ , where 32 is the maximal length of the group. For each of these groups HOSVD calculates three orthonormal transform matrices (dictionaries) of sizes  $8 \times 8$ ,  $8 \times 8$  and  $32 \times 32$ .

In Fig.12 we show an example of these transform matrices as they are calculated for the  $128 \times 128$  image with cameraman for phase and Lena for amplitude in the noiseless scenario. Small rectangles in Fig.12 are  $8 \times 8$  transforms applied to the vertical columns of  $3D$  groups. We use *red* for phases and *blue* for amplitudes of these complex-valued transforms. Fig.12 qualitative illustrates a variety of the transforms generated in CD-BM3D. Each of these  $8 \times 8$  transforms is built

for non-local areas of patches similar to the corresponding reference patch.

The number of these transforms, 1681 in this image, is equal to the total  
655 number of the reference patches. Remind that not all pixels are used to define  
reference patches. In the considered test it is every third pixels in each row  
and each column. The ratio of the total number of the reference patches to the  
image size is  $128 \cdot 128 / 1681 \simeq 10$ .

Thus, for the  $128 \times 128$  image we calculate 1681 HOSVD transforms. For  
660 each 3D group we have the core tensor of the maximal size  $8 \times 8 \times 32 = 2048$   
with the total number of the spectral elements (elements of the core tensors)  
for the image equal to  $2048 \cdot 1681 = 3442688$ .

Compared with the image size  $128 \times 128 = 16384$  the HOSVD spectral repre-  
sentation enables a huge redundancy in the transform domain,  $3442688 / 16384 \simeq$   
665 200. However, after thresholding the total number of the non-zero (active) spec-  
tral elements is about 11090. Thus the ratio  $3442688 / 11090 \simeq 300$  is the sparsity  
achieved in the spectral domain.

These calculations clarify explicitly what kind of sparsity is appeared in the  
developed algorithms. For image analysis the huge overcomplete number of the  
670 spectral elements are produced and only tiny part of them is used for imaging  
as they are selected by the thresholding procedures.

In this test the ratio of the number of active spectral elements to the image  
size is  $16384 / 11090 \simeq 1.5$ . The main goal of this sparsity development is the  
image quality but not the image compression.

675 Fig.13 is the distribution (histogram) of the active spectral elements: a num-  
ber of groups (vertical axis) generated by CD-BM3D versus a number of the  
active spectral elements (horizontal axis). This distribution has a maximum at  
10 showing that 140 groups have 10 active spectral components. Numbers of  
the groups having smaller or larger values of the active spectral items can be  
680 very small.

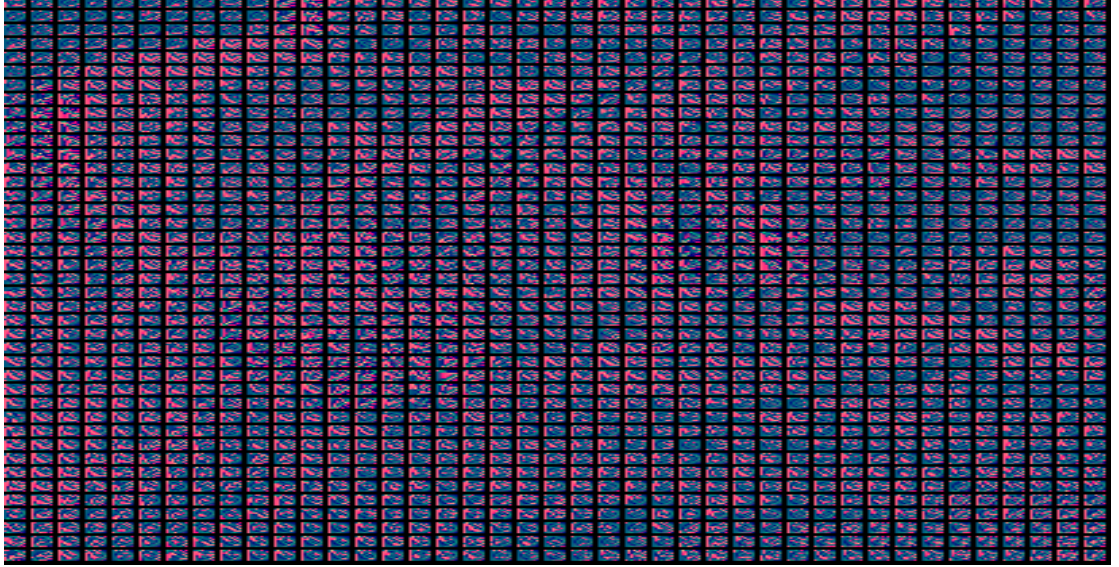


Figure 12: Complex-valued  $8 \times 8$  transform matrices for noiseless data with varying phase (cameraman) and varying amplitude (Lena). Visualization is produced by red and blue colours, respectively, for angles and amplitudes of elements of the complex-valued transforms.

## 5. Concluding remarks

This paper introduces CD-BM3D and iterative CD-BM3D, as effective algorithms for interferometric phase image estimation, that is, the estimation of phase modulo- $2\pi$  images from sinusoidal  $2\pi$ -periodic and noisy observations. The problem is formulated as estimation of the true complex-valued image via spectral sparse representation for 3D grouped data. Complex domain spectral representations of these BM3D groups are obtained by HOSVD factorization of the 3D data. The filtering of the HOSVD spectrum is produced using component wise hard-thresholding. In a series of experiments with simulated data, CD-BM3D and iterative CD-BM3D algorithms mainly produced better estimates than the SpInPhase and WFT algorithms which are the state-of-the-art in the field.

Through the extensive testing we found that CD-BM3D is a nonexpansive operator. This observation is a base for the convergence proof for iterative

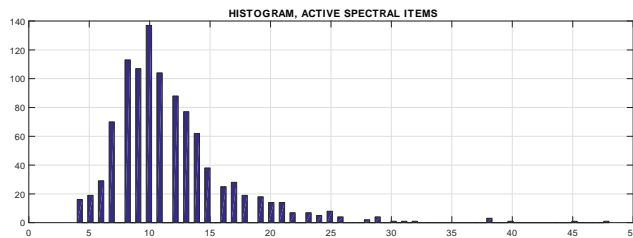


Figure 13: Histogram of the number of active (nonzero) elements of the core (spectral) tensor,  $\sigma = 0.5$ , phase image mountains and amplitude is equal to 1.

695 CD-BM3D.

The following versions of the CD-BM3D algorithms have been tested in process of the algorithm's development: soft-thresholding in CD-BM3D and 2D SVD transform instead of 3D HOSVD. It is found that the hard-thresholding and 3D HOSVD enable better performance.

700 The complex domain BM3D-style Wiener filtering as a postprocessing for CD-BM3D was developed and tested. It was found that this algorithm demonstrates an improvement in performance with respect to the CD-BM3D with PSNR results between those for CD-BM3D and iterative CD-BM3D.

705 Further development of the obtained results concerns to application of these novel algorithms and their modifications for the problems with the real-valued observations where the complex domain denoising appeared as a sub-problem imbedded in complex iterative procedures.

## 6. Acknowledgement

This work is supported by the Academy of Finland, project no. 138207, 710 2015-2019. The authors are thankful to Alessandro Foi for fruitful discussions.

## References

- [1] R. K. Tyson. *Principles of Adaptive Optics*. 4rd ed., CRC Press, 2014.

- [2] L. Wang and H. Wu. *Biomedical Optics: Principles and Imaging*. John Wiley & Sons, Inc., 2007.
- 715 [3] B. Kress and P. Meyrueis. *Applied Digital Optics: From Micro-Optics to Nanooptics*. John Wiley & Sons, Inc., 2009.
- [4] A. Patil and P. Rastogi, "Moving ahead with phase," *Optics and Lasers in Engineering*, vol. 45, no. 2, pp. 253-257, 2007.
- [5] Th. Kreis, *Handbook of Holographic Interferometry*. Wiley-VCH, Berlin, 720 2005.
- [6] J. Glückstad, and D. Palima. *Generalized phase contrast: applications in optics and photonics*. Springer Series in Optical Sciences, vol. 146, 2009.
- [7] M. Elad. *Sparse and Redundant Representations: from Theory to Applications in Signal and Image Processing*. Springer, 2010.
- 725 [8] S. Gazit, A. Szameit, Y. C. Eldar, M. Segev, "Super-resolution and reconstruction of sparse sub-wavelength images, " *Optics Express* **17**, pp. 23920-23946, 2009.
- [9] Y. Shechtman, Y. C. Eldar, O. Cohen, H. N. Chapman, J. Miao, and M. Segev, "Phase retrieval with application to optical imaging: a contemporary overview," *IEEE Signal Processing Magazine*, pp. 87-109, 730 2015.
- [10] Z. Xu and E. Y. Lam , "Image reconstruction using spectroscopic and hyperspectral information for compressive terahertz imaging", *J. Opt. Soc. Am. A*, **27**, Issue 7, pp. 1638-1646, 2010.
- [11] V. Katkovnik and J. Astola, " High-accuracy wavefield reconstruction: decoupled inverse imaging with sparse modeling of phase and amplitude, " *J. Opt. Soc. Am. A*, **29**, pp. 44 – 54, 735 2012.
- [12] V. Katkovnik and J. Astola, "Sparse ptychographical coherent diffractive imaging from noisy measurements," *J. Opt. Soc. Am. A*, vol. 30, 367-379, 2013.

- 740 [13] V. Katkovnik and J. Astola, “Compressive sensing computational ghost imaging,” *J. Opt. Soc. Am. A*, vol. 29, no. 8, pp. 1556-1567, 2012.
- [14] A. Bourquard, N. Pavillon, E. Bostan, C. Depeursinge, and M. Unser, “A practical inverse-problem approach to digital holographic reconstruction,” *Optics Express*, **21**, no. 3, pp. 3417-3433, 2013.
- 745 [15] A. Danielyan, A. Foi, V. Katkovnik, and K. Egiazarian, “Spatially adaptive filtering as regularization in inverse imaging: Compressive sensing, super-resolution, and upsampling,” *Super-Resolution Imaging* (P. Milanfar, ed.), CRC Press/Taylor, pp. 123–153, 2010.
- [16] F. Heide, M. Steinberger, Y.-T. Tsai, M. Rouf, D. Pajak, D. Reddy, O. Gallo, J. Liu, W. Heidrich, K. Egiazarian, et al., “Flexisp: A flexible camera image processing framework,” *ACM Transactions on Graphics (TOG)*, vol. 33, no. 6, p. 231, 2014.
- 750 [17] S. Sreehari, S. Venkatakrisnan, B. Wohlberg, L. F. Drummy, J. P. Simmons, and C. A. Bouman, “Plug-and-play priors for bright field electron tomography and sparse interpolation,” arXiv preprint arXiv:1512.07331, 2015.
- [18] C. A. Metzler, A. Maleki and R. G. Baraniuk, “BM3D-PRGAMP: Compressive phase retrieval based on BM3D denoising,” *Proceedings of IEEE International Conference on Image Processing (ICIP)*, 2016.
- 760 [19] K. Dabov, A. Foi, V. Katkovnik, and K. Egiazarian, “Image denoising by sparse 3D transform-domain collaborative filtering,” *IEEE Trans. Image Process.*, **16**, no. 8, pp. 2080-2095, 2007.
- [20] L. De Lathauwer, B. De Moor, J. Vandewalle, “A multilinear singular value decomposition,” *SIAM J. Matrix Anal. Appl.* **21**, pp. 1253–1278, 2000.
- 765 [21] L.R. Tucker, “Some mathematical notes on three-mode factor analysis,” *Psychometrika* **31**, pp. 279–311, 1966.

- [22] P.M. Kroonenberg, J. De Leeuw, "Principal component analysis of three-mode data by means of alternating least squares algorithms," *Psychometrika* 45 (1) pp. 69–97, 1980.
- 770 [23] Foi, A., V. Katkovnik, and K. Egiazarian, "Pointwise shape-adaptive DCT for high-quality denoising and deblocking of grayscale and color images", *IEEE Trans. Image Process.*, **16**, no. 5, pp. 1395-1411, 2007.
- [24] A. Rajwade, A. Rangarajan and A. Banerjee, "Image denoising using the higher order singular value decomposition," *IEEE Trans. on Pattern Analysis and Machine Intelligence*, **35**, no. 4, pp. 849-862, 2013.
- 775 [25] H. Hongxing, J. M. Bioucas-Dias, and V. Katkovnik, "Interferometric phase image estimation via sparse coding in the complex domain," *IEEE Trans. on Geoscience and Remote Sensing*, vol. 53, no. 5, pp. 2587 - 2602, 2015.
- [26] V. Katkovnik, K. Egiazarian, J. Bioucas-Dias, 'Phase imaging via sparse coding in the complex domain based on high-order SVD and nonlocal BM3D techniques,' *Proceedings of IEEE International Conference on Image Processing (ICIP 2014)*, pp. 4587-4591, 2014.
- 780 [27] D. Donoho and I. Johnstone, "Ideal spatial adaptation by wavelet shrinkage," *Biometrika*, vol. 81, pp. 425-455, 1993.
- [28] D. C. Ghiglia and M. D. Pritt. *Two-Dimensional Phase Unwrapping: Theory, Algorithms, and Software*. Wiley, 1998.
- 785 [29] A. Danielyan, V. Katkovnik, and K. Egiazarian, " BM3D frames and variational image deblurring, " *IEEE Trans. Image Process.*, **21**, pp. 1715 – 1728, 2012.
- [30] M. Elad, P. Milanfar, and R. Rubinstein, Analysis versus synthesis in signal priors, *Inverse Problems*, **23**, no. 3, pp. 947-968, 2007.
- 790 [31] K. Leyton-Brown and Y. Shoham, Essentials of Game Theory: A Concise Multidisciplinary Introduction, ser. Synthesis Lectures on Artificial Intelli-

gence and Machine Learning. San Francisco, CA: Morgan Claypool Publ.,  
2008.

795

- [32] F. Facchinei and C. Kanzow, “Generalized Nash equilibrium problems,”  
*4OR, Quart. J. Oper. Res.*, vol. 5, no. 3, pp. 173–210, 2007. vQ. Kemaο,  
“Two-dimensional windowed Fourier transform for fringe pattern analy-  
sis: Principles, applications and implementations,” *Optics and Lasers in*  
800 *Engineering*, vol. 45, no. 2, pp. 304 – 317, 2007.

- [33] D. Bertsekas, *Constrained optimization and lagrange multiplier methods*.  
Belmont, MA: Athena Scientific, 1996.

- [34] Q. Kemaο, Q., *Windowed fringe pattern analysis*. SPIE Press, (2013).

- [35] J. M. Bioucas-Dias and G. Valadão, “Phase unwrapping via graph cuts,”  
805 *IEEE Trans. Image Process*, **16**, no. 3, pp. 698–709, 2007.

- [36] M. Zhao, Q. Kemaο, ” A comparison study of denoising techniques in fringe  
pattern analysis,” *Internal. Conf. on Experimental Mechanics*, 2014, Proc.  
of SPIE vol. 9302, 930208-1-930208-6, 2014.

Table 2: ACCURACY OF PHASE AND AMPLITUDE RECONSTRUCTION: CD-BM3D (BM<sub>1</sub>), CD-BM3D ITERATIVE (BM<sub>2</sub>), SpInPhase (Sp) AND WFT.

Surf.	PSNR <sub><math>\varphi</math></sub>				RMSE <sub><math>\varphi_{abs}</math></sub>				PSNR <sub><math>ampl</math></sub>				
	$\sigma$	BM <sub>1</sub>	BM <sub>2</sub>	Sp	WFT	BM <sub>1</sub>	BM <sub>2</sub>	Sp	WFT	BM <sub>1</sub>	BM <sub>2</sub>	Sp	WFT
Trunc. Gauss.	.1	50.42	<b>50.94</b>	48.06	47.56	.019	<b>.018</b>	.025	.026	35.61	<b>36.15</b>	31.84	18.46
	.3	43.86	<b>44.44</b>	42.05	40.25	.040	<b>.037</b>	.050	.061	28.28	<b>28.98</b>	26.05	17.06
	.5	39.66	<b>40.00</b>	38.76	36.69	.065	<b>.060</b>	.072	.091	23.91	<b>24.96</b>	23.24	15.71
	.7	36.57	<b>37.46</b>	36.08	34.23	.678	<b>.083</b>	.364	.63	20.93	<b>22.32</b>	20.44	14.70
	.9	33.86	<b>33.89</b>	33.47	32.24	1.11	1.11	<b>.315</b>	1.49	18.28	<b>20.58</b>	15.99	13.83
Shear plane	.1	56.90	<b>58.17</b>	58.01	48.25	.009	<b>.007</b>	.008	.024	40.58	41.88	<b>43.06</b>	18.45
	.3	48.73	<b>49.44</b>	49.02	40.93	.028	.023	<b>.021</b>	.056	31.04	32.60	<b>32.86</b>	17.08
	.5	44.37	<b>46.66</b>	43.65	37.36	.038	<b>.029</b>	.043	.085	27.80	<b>30.22</b>	26.77	15.76
	.7	41.46	<b>43.97</b>	40.15	35.06	.053	<b>.040</b>	.061	.111	24.73	<b>27.44</b>	21.71	14.77
	.9	39.05	<b>41.78</b>	33.65	33.17	.070	<b>.051</b>	.131	.138	22.19	<b>25.21</b>	14.28	13.92
Sinus. cont.	.1	56.65	<b>57.98</b>	56.26	43.87	.009	<b>.008</b>	.009	.043	40.58	<b>41.71</b>	37.65	17.88
	.3	47.09	<b>48.54</b>	47.92	35.84	.028	<b>.023</b>	.025	.102	28.14	29.26	<b>32.91</b>	15.30
	.5	42.25	<b>44.05</b>	43.22	32.09	.048	<b>.039</b>	.043	.161	23.81	24.99	<b>27.32</b>	13.36
	.7	38.52	<b>40.85</b>	40.68	29.41	.074	<b>.057</b>	.058	.226	20.46	22.27	<b>24.78</b>	11.63
	.9	35.48	<b>37.86</b>	36.29	27.29	.105	<b>.080</b>	.096	.315	17.41	20.04	<b>22.08</b>	10.24
Sinus. disc.	.1	55.53	<b>56.40</b>	48.08	43.87	.010	<b>.010</b>	.024	.04	39.58	<b>40.59</b>	30.71	18.06
	.3	45.85	<b>46.34</b>	44.16	35.84	.032	<b>.030</b>	.037	.10	29.86	<b>30.41</b>	27.59	15.78
	.5	41.33	<b>42.00</b>	39.54	32.09	.054	<b>.050</b>	.057	.16	25.31	<b>25.78</b>	24.63	14.01
	.7	38.00	<b>38.72</b>	36.08	29.41	.079	<b>.730</b>	.092	.21	22.34	<b>22.71</b>	21.17	12.50
	.9	35.2	<b>36.34</b>	33.93	27.29	.109	<b>.095</b>	.125	.29	19.95	<b>20.67</b>	19.07	11.14
Mount.	.1	46.03	<b>46.84</b>	46.20	46.81	.031	<b>.028</b>	.030	.028	30.69	<b>31.75</b>	31.02	18.45
	.3	40.99	<b>41.25</b>	40.32	39.54	.056	<b>.053</b>	.061	.066	25.39	<b>25.56</b>	25.07	16.98
	.5	36.73	<b>37.04</b>	36.84	35.97	.091	<b>.088</b>	<b>.088</b>	.100	21.42	<b>21.73</b>	21.71	15.63
	.7	33.86	<b>34.37</b>	33.20	33.51	.127	<b>.120</b>	.123	.132	18.75	<b>19.34</b>	18.99	14.56
	.9	31.54	<b>32.31</b>	31.25	31.63	.166	0.152	<b>.149</b>	.165	16.31	<b>17.43</b>	16.47	13.59

Table 3: ACCURACY OF PHASE AND AMPLITUDE RECONSTRUCTION: CD-BM3D ( $BM_1$ ), CD-BM3D ITERATIVE ( $BM_2$ ), SpInPhase (Sp) AND WFT.

Image		PSNR $_{\varphi}$				PSNR $_{ampl}$			
		$\sigma$	$BM_1$	$BM_2$	Sp	WFT	$BM_1$	$BM_2$	Sp
Lena	.1	45.66	<b>46.17</b>	41.43	45.42	35.61	34.39	<b>38.24</b>	22.31
	.3	39.64	<b>40.29</b>	38.48	39.16	29.89	29.13	<b>31.31</b>	20.61
	.5	36.89	<b>37.67</b>	36.73	36.30	26.42	26.61	<b>29.40</b>	19.01
	.7	35.02	<b>35.87</b>	34.44	34.42	23.86	24.66	<b>27.25</b>	17.73
	.9	33.71	<b>34.55</b>	34.14	32.93	21.76	23.07	<b>24.69</b>	16.60
Cameraman	.1	44.06	<b>44.53</b>	41.00	43.79	35.50	34.60	<b>36.22</b>	22.21
	.3	39.02	<b>39.56</b>	37.89	38.00	29.45	29.20	<b>29.75</b>	20.50
	.5	36.30	<b>37.04</b>	35.97	35.35	26.07	26.38	<b>28.81</b>	18.86
	.7	34.41	<b>35.25</b>	34.17	33.59	23.60	<b>24.51</b>	26.49	17.61
	.9	33.11	<b>33.92</b>	33.28	32.21	21.60	<b>23.04</b>	23.00	16.51

Table 4: COMPUTATION TIME IN SEC. ALGORITHMS: CD-BM3D ( $BM_1$ ), CD-BM3D ITERATIVE ( $BM_2$ , 5 ITERATIONS), SpInPhase (Sp) AND WFT

Im. Size \ Alg.	$BM_1$	$BM_2$	Sp	WFT
$100 \times 100$	4.2	18.3	81.8	10.6
$256 \times 256$	27.6	136.2	100.3	23.0
$512 \times 512$	120.2	603.5	216.4	117.4
$1024 \times 1024$	465	2330	1503	419